

Electrostatic determinants of voltage sensitivity in ion channels: Simulations of sliding-helix mechanisms

December 20, 2011

Alexander Peyser* Wolfgang Nonner*

*Department of Physiology and Biophysics, University of Miami

Abstract

Electrical signaling via voltage-gated ion channels depends upon the function of the voltage sensor (VS), identified with the S1–S4 domain of voltage-gated K channels. Here we investigate some physical aspects of the sliding-helix model of the VS using simulations based on VS charges, linear dielectrics and whole-body motion. Model electrostatics in voltage-clamped boundary conditions are solved using a boundary element method. The statistical mechanical consequences of the electrostatic configurational energy are computed to gain insight into the sliding-helix mechanism and to predict experimentally measured ensemble properties such as gating charge displaced by an applied voltage. Those consequences and ensemble properties are investigated for variations of: S4 configuration (α - and 3_{10} -helical), intrinsic counter-charges, protein polarizability, geometry of the gating canal, screening of S4 charges by the baths, and protein charges located at the bath interfaces. We find that the sliding helix VS has an inherent electrostatic stability and its function as a VS is robust in the parameter space explored. Maximal charge displacement is limited by geometry, specifically the range of movement where S4 charges and counter-charges overlap in the region of weak dielectric. The steepness of charge rearrangement in the physiological voltage range is sensitive to the landscape of electrostatic energy: energy differences of <2 kT have substantial consequences. Such variations of energy landscape are produced by all variations of model features tested. The amount of free energy per unit voltage that a sliding-helix VS can deliver to other parts of the channel (conductance voltage sensitivity) is limited by both the maximal displaced charge and the steepness of charge redistribution by voltage (sensor voltage sensitivity).

Introduction

Electrical excitability of cells is possible because the movement of a few charges can control the flow of many charges. This principle — amplification — led Hodgkin and Huxley (1952) to their theory of the action potential in terms of electrically controlled membrane conductances. Electrically controlled conductances have been localized to channel proteins conducting sodium, potassium or calcium ions across the cell membrane. Voltage-controlled ionic conductances and underlying intrinsic charge movements of ion channels have been studied experimentally for many years (reviewed by Hille, 2001). Electrophysiology has been complemented in more recent years by techniques measuring channel topology, channel structure and the change in channel function (reviewed by Gandhi and Isacoff, 2002; Catterall, 2010). Together, these perspectives provide a wealth of detailed information on the ‘voltage sensor’ (VS) common to these channels and exemplified by the S1–S4 transmembrane domains of *Shaker*-type K^+ channels. Here we use computation to identify physical properties that are important for voltage sensing, with a natural focus on electrostatic properties.

Site-directed mutagenesis experiments have shown that only a limited number of amino acid residues of a voltage-dependent ion channel are individually important for voltage sensitivity (Gandhi and Isacoff, 2002). To study VS electrostatics, we use models in which amino acids are not made explicit. Since amino-acid residues with charged side-chains in S4 as well as S2 and S3 transmembrane segments strongly determine VS function (Papazian et al., 1995), we explicitly represent those charges. These charged groups operate in vivo in an environment composed of materials of diverse electrical polarizabilities. We distinguish three such materials in the model (membrane lipid, baths, and protein) and describe electrical polarizabilities by dielectric coefficients that are uniform within each region.

The electrostatic model constructed from point charges and piecewise uniform dielectrics is encapsulated by conductors clamped to imposed potentials from external sources while external charge flow is monitored. Thus the model is coupled to the macroscopic electrical setup of a ‘voltage clamp’ experiment. The electrostatics of the system composed of the VS model and the electrode setup is solved self-consistently. The configuration space of the model VS is systematically sampled to construct a partition function based on electrostatic configurational energy. Using this partition function, we compute ensemble expectations of observable random variables (e.g., of gating charge displaced at an applied voltage). This way our theoretical results meet two criteria for practical usefulness: they are consistent solutions of the physics included in the model, and they directly pertain to macroscopic experimental results.

The purpose of our simulations is to elucidate how physical features of the VS determine functional characteristics. To this end, we determine the consequences of varying electrostatic and geometrical parameters of VS models.

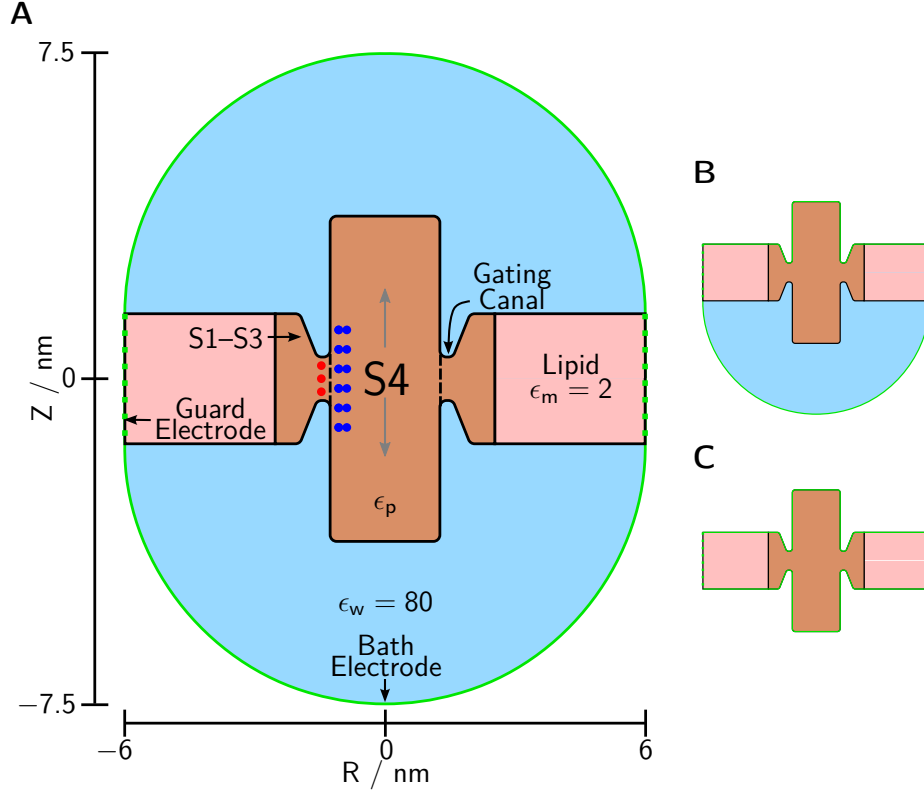
Model and boundary conditions

We test VS models in a simulated voltage clamp setup (Fig. 1, further geometrical information is given in Table 1). The simulation cell is represented by an axial cross-section of the radially symmetric three-dimensional domain swept by rotating that cross-section about its vertical axis. The external boundaries (in green) are electrode surfaces kept at controlled electrical potentials. The blue zones represent aqueous baths (with a dielectric coefficient $\epsilon_w = 80$). The pink zone is a region of small dielectric coefficient ($\epsilon_m = 2$) that represents the lipid membrane. The brown zone represents the region of the channel protein that we model; this region is assigned a dielectric coefficient of $\epsilon_p = 4$ unless noted otherwise. These dielectrics are piecewise uniform and therefore have sharp boundaries (solid black lines). Point charges representing protein charges of interest are embedded in the region of protein dielectric. Variation of their placement is part of this study and will be detailed later. The protein region as seen here represents the matrix of the S4 helix as a central cylinder, surrounded by the other parts of the channel that create as well a dielectric environment different from the dielectric environment of the membrane lipid. Included in the ‘protein’ region are the invaginations which allow the baths to extend into the planes defining the lipid phase of the membrane. The radius of the S4 dielectric matrix is 1 nm (α -helix) or 0.98 nm (3_{10} -helix).

Point charges representing protein charges are arranged at a minimal distance of 0.2 nm from the protein/water boundary. The charged guanido group of each arginine residue of the S4 segment is represented as three point charges of $1/3 e_0$ on a circle of radius 0.122 nm (blue spheres in Fig. 2). The centers of the S4 arginine charges are arranged on a helix defined by arginine side chains on an α - or 3_{10} -helix backbone, where every third amino acid is an arginine. For the α -helix, charged residues are separated by 0.45 nm in the transmembrane direction and 60° leftward around the helix; for the 3_{10} -helix, charged residues are separated by 0.6 nm and 0° .

Dimensions of the simulation surfaces are varied within those constraints as defined in Table 1. Part A maps the topology of the protein and membrane surface of Fig. 1 onto metrics for simulations, defined in part B of the table. Since the surfaces in the system are radially symmetrical and smooth, the system can be defined by a set of inflection points with their curvature on the left half of the system to be simulated. When the gating canal is symmetrical, this reduces further to the upper half of the left side. (As illustrated with Figs. 1A–C and discussed later in “Results” under “Screening of VS charges”, these metrics apply for “dilute” systems with electrodes far from the membrane surface, “infinitely concentrated” systems with electrodes on the membranes, and asymmetrical systems with a dilute side and a concentrated side.)

We analyze two degrees of freedom for VS charge movement: the curve on which (triplets of) S4 charge centers are aligned can be both translated along the helix axis and rotated about that axis. The model S4 charges thus move like parts of a solid body. Negatively charged residues contributed by the S2 and S3 transmembrane segments of the natural VS are modeled as point charges of $-1 e_0$



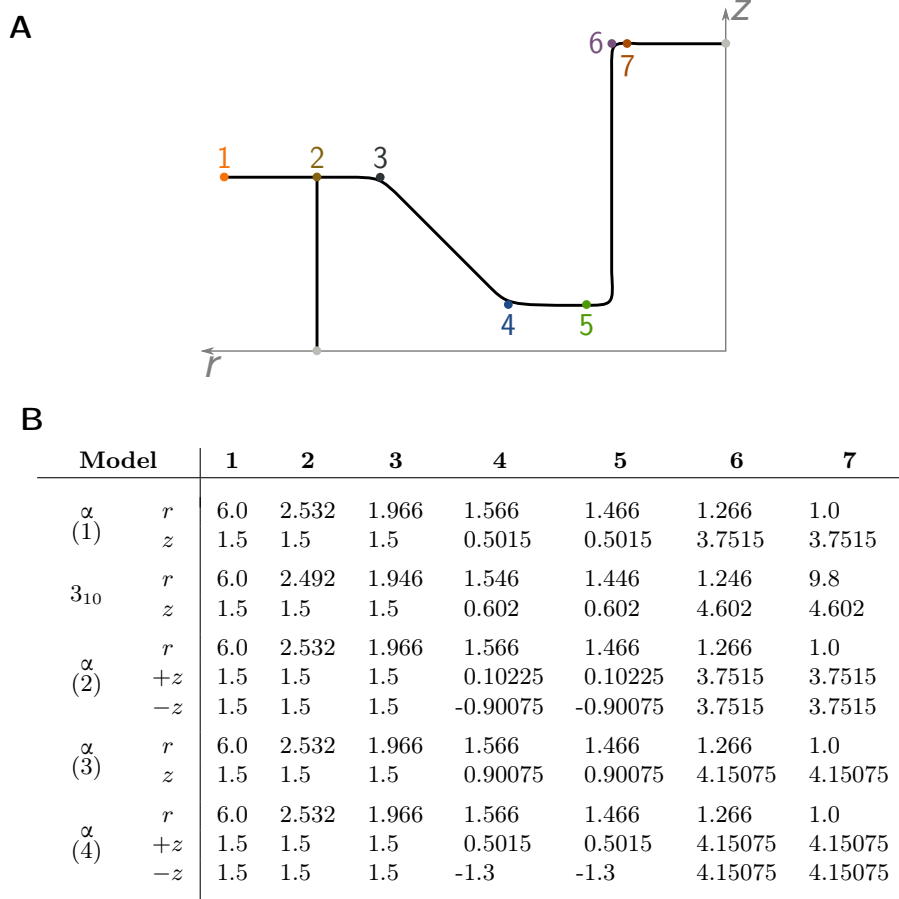


Table 1: *Geometrical parameters of models.* (A): Mapping from geometrical positions in Figure 1 to indexed geometrical parameters. Inflection points and lengths are varied among different models, depending on counter-charge positions, helix conformation and gating pore size. Positions in r (radial) and z (axial) coordinates are marked by a colored point and an associated number. All corners are rounded with curvature radius of 0.15 nm. Points 1,2,3,4, and 6 define the profile of the lipid and protein dielectrics, from the outermost end of the lipid domain (1) to the face of the S4 cylinder (6). Point 5 marks the radial position assigned to counter-charges, point 7 the radial position of S4 charges. (B): Coordinates (in nm) of the points defining membrane and protein metrics. For models with symmetrical gating canal, r and z define both the extracellular and intracellular surfaces. For models with an asymmetric gating canal, $+z$ values are used for the extracellular surface and $-z$ for the intracellular surface. These metrics apply regardless of electrode positioning. The numbers in parentheses listed in the first column refer to the variants of gating canal geometry used in the models for Fig. 8. See Figs. S3–S6 for 3 dimensional representations of some geometries.

arranged on a curve parallel to the curve on which S4 charges are centered (red spheres in Fig. 2); the offset from the helix axis of the counter-charge curve is 0.466 nm larger than the radius of the curve of the centers of the (triplets of) S4 charges (see Table 1). The axial and angular intervals between counter-charges are chosen so that at most one S4 charge can exactly line up with any of the three counter-charges (see legend of Fig. 2). Counter-charges are stationary in their assigned positions.

We design the simulation to address physical questions with computational efficiency. For instance, the electrodes encapsulating the simulation cell serve three purposes:

1. The bath electrodes provide Dirichlet boundary conditions corresponding to a voltage clamp. Our formulation of the electrostatics (described in the next section) establishes these conditions.
2. The electrodes substitute for screening by bath ions of uncompensated protein charge. Screening by the ions in an aqueous bath is equivalent to the screening provided by charge on a metal foil placed in the water a distance away from the protein boundary. According to the Debye-Hückel theory approximation, an electrode distance of ≈ 0.8 nm corresponds to physiological bath ionic strength. The electrode location shown in Fig. 1A thus corresponds to a bath solution in the low millimolar range. An alternate configuration, a simulation cell with the bath regions omitted and the electrodes placed directly on the membrane and protein boundaries (Fig. 1C), establishes screening at the Onsager limit (approached at exceedingly large ionic strength). Results obtained with the two alternate electrode placements allow us to examine the possible range of screening effects at far smaller computational cost than the costs of a simulation with explicit bath ions.
3. At the surface where the membrane region meets the cell boundary, a set of guard electrodes forming rings around the cell maintain a graded potential which varies between the potentials applied at the inner and outer bath electrodes. These guard electrodes impose at the membrane edge a potential similar to the potential existing in a macroscopic system at a location far from the protein.

Translational and rotational motions of the S4 helix are simulated by allowing the ensemble of S4 charges to slide within the dielectric envelope provided by the S4 matrix shown in Fig. 1. The protein dielectric itself does not accompany the movement of the charges. With the S4 dielectric matrix extended far enough into the baths, keeping the S4 dielectric stationary has negligible electrostatic consequences because the dielectric of the model is uniform within the S4 matrix. Simulating S4 motion this way reduces computational effort of model exploration by several orders of magnitude.

A simulation setup as shown in Fig. 1 tests a single VS that is not interacting with other parts of the channel protein, in particular the parts mediating the

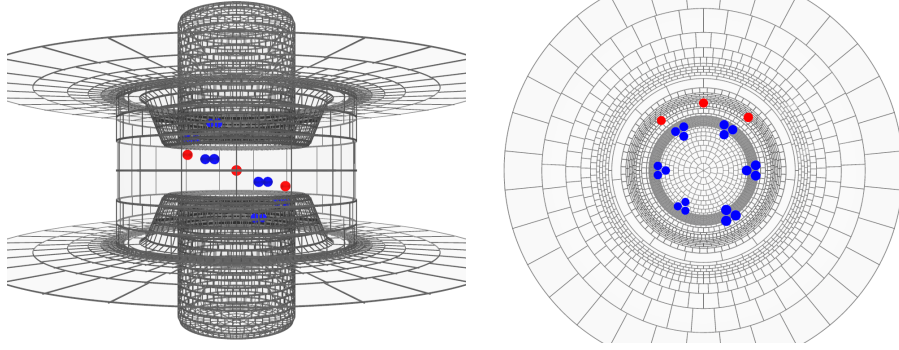


Figure 2: *VS charge positions and dielectric boundary surfaces in a α -helical model. Blue symbols: S4 charges, each represented as three point charges of $1/3 e_0$; red symbols: counter-charges in the S2 and S3 segments, each represented as a single point charge of $-1 e_0$. The dielectric boundary surface is divided into curved tiles whose magnitudes are varied depending on their distance from point charges and local curvature. This is the surface grid used in solving the induced-charge calculation. This figure is drawn using perspective-enhancing features. For the range of motion of the S4 in this model, see the animated Animation S1.*

gating of the conductive pore. This model VS thus operates as an ‘idling’ transducer of electrical force. The forces acting between a VS and other parts of the natural channel are not known. The reactions of model voltage-sensors to such forces can be explored by simulations which include hypothesized force fields in addition to the electrostatic force field. Characteristics of the ‘load’ acting on the actual VS may be inferred in this manner. However, here we report simulations of the idle VS.

Methods

Electrostatics

We are concerned with electrostatic interactions among charged groups of the VS protein, electrode charges and charges induced on sharp dielectric boundaries. In solving the electrostatics we take advantage of the fact that all other charges besides the point charges of the protein are distributed on a few boundary surfaces rather than distributed throughout a volume. The primary task of calculating electrostatic interactions consists in determining the charge distributions on the electrode and dielectric boundaries, distributions which are initially unknown for a given configuration of protein charges and applied voltage.

Computation of unknown charges

Boda et al. (2006) have described and tested a boundary element method (Induced Charge Calculation, ICC) for computing the charge distribution on the dielectric boundaries of a system consisting of point charges and linear isotropic dielectrics with sharp boundaries. We include as additional electrostatic element the ‘electrode’. This element is an infinitesimally thin conductive foil charged to a prescribed electric potential using an external source. In our system, this surface is also a dielectric boundary between the simulation cell and the dielectric surrounding the cell (e.g., vacuum). Thus the charge of an electrode is in part induced charge (as in Boda et al.) and source charge (to fix the prescribed potential). In the following we show how the total electrode charge can be calculated without needing to separately calculate its parts. The electrode charge calculation complements the induced charge calculation, making it possible to calculate all the initially unknown charges in the system.

The spatial density of source charge ρ^{src} in our system is composed of the point source charges q_k^{src} of the VS protein located at positions \mathbf{r}_k and source charge distributed on the electrodes \mathcal{E} with surface density $\sigma^{\text{src}}(\mathbf{r} \in \mathcal{E})$.

The polarization charge density induced at any location \mathbf{r} in a dielectric is

$$\rho^{\text{ind}}(\mathbf{r}) = \frac{1 - \epsilon(\mathbf{r})}{\epsilon(\mathbf{r})} \rho^{\text{src}}(\mathbf{r}) - \epsilon_0 \frac{\nabla \epsilon(\mathbf{r})}{\epsilon(\mathbf{r})} \cdot \mathbf{E}(\mathbf{r}) \quad (1)$$

where ϵ is the generally location-dependent dielectric coefficient, ϵ_0 the permittivity of the vacuum, and \mathbf{E} the electric field strength produced by all (source and induced) charges in the system. This relation follows from Poisson’s equation (including polarization) and the constitutive relation describing polarization in a linear, isotropic dielectric (Boda et al., 2006). The first term on the right-hand side of Eq. 1 describes the charge induced on the surfaces of the volume element at \mathbf{r} if the element contains source charge. The second term describes charge induced in the volume element by the electric field if the dielectric coefficient at \mathbf{r} has a non-zero gradient.

For our charge calculations, we combine collocated source and induced charges into an effective charge for computing the field and potential. The effective

charge density associated with a known source charge density $\rho^{\text{src}}(\mathbf{r})$ embedded in a dielectric (described by a locally uniform $\epsilon(\mathbf{r})$) is:

$$\rho^{\text{eff}}(\mathbf{r}) = \frac{\rho^{\text{src}}(\mathbf{r})}{\epsilon(\mathbf{r})} \quad (2)$$

The effective charge density of an electrode includes both contributions to induced charge described by Eq. 1, as well as the source charge.

The dielectric boundaries \mathcal{B} inside the simulation cell (marked in *black* in Fig. 1) do not carry source charge. However, the electric field in the simulation cell induces the charge density $\sigma^{\text{ind}}(\mathbf{r})$ at locations $\mathbf{r} \in \mathcal{B}$. This induced charge density is initially unknown.

The field strength \mathbf{E} and potential V in our system are produced by the superposition of the fields and potentials of the source and induced charges:

$$\begin{aligned} \mathbf{E}(\mathbf{r}) = & \frac{1}{4\pi\epsilon_0} \sum_k q_k^{\text{eff}} \frac{\mathbf{r} - \mathbf{r}_k}{|\mathbf{r} - \mathbf{r}_k|^3} \\ & + \frac{1}{4\pi\epsilon_0} \int_{\mathcal{B}} \sigma^{\text{ind}}(\mathbf{r}') \frac{\mathbf{r} - \mathbf{r}'}{|\mathbf{r} - \mathbf{r}'|^3} da' + \frac{1}{4\pi\epsilon_0} \int_{\mathcal{E}} \sigma^{\text{eff}}(\mathbf{r}') \frac{\mathbf{r} - \mathbf{r}'}{|\mathbf{r} - \mathbf{r}'|^3} da' \end{aligned} \quad (3)$$

$$\begin{aligned} V(\mathbf{r}) = & \frac{1}{4\pi\epsilon_0} \sum_k q_k^{\text{eff}} \frac{1}{|\mathbf{r} - \mathbf{r}_k|} \\ & + \frac{1}{4\pi\epsilon_0} \int_{\mathcal{B}} \sigma^{\text{ind}}(\mathbf{r}') \frac{1}{|\mathbf{r} - \mathbf{r}'|} da' + \frac{1}{4\pi\epsilon_0} \int_{\mathcal{E}} \sigma^{\text{eff}}(\mathbf{r}') \frac{1}{|\mathbf{r} - \mathbf{r}'|} da' \end{aligned} \quad (4)$$

where da' is the area of the surface element at location \mathbf{r}' .

The unknown induced surface charge density at the dielectric boundary is related to the field strength by (Boda et al., 2006):

$$\sigma^{\text{ind}}(\mathbf{r}) = -\frac{\Delta\epsilon(\mathbf{r})}{\bar{\epsilon}(\mathbf{r})} \epsilon_0 \mathbf{n}(\mathbf{r}) \cdot \mathbf{E}(\mathbf{r}) \quad (5)$$

where \mathbf{r} is any location on the surface \mathcal{B} , $\Delta\epsilon(\mathbf{r})$ is the change of dielectric coefficient in the normal direction $\mathbf{n}(\mathbf{r})$ of the dielectric boundary, and $\bar{\epsilon}(\mathbf{r})$ is the mean of the dielectric coefficients at the boundary location.

The potential at any location \mathbf{r} on the electrode surfaces \mathcal{E} has a value $V^{\text{VC}}(\mathbf{r})$ imposed by the voltage clamp:

$$V(\mathbf{r}) = V^{\text{VC}}(\mathbf{r}) \quad (6)$$

Inserting the expression for the electric field strength from Eq. 3 into Eq. 5 and inserting the expression for the electric potential from Eq. 4 into Eq. 6 yields two integral equations in terms of both $\sigma^{\text{ind}}(\mathbf{r} \in \mathcal{B})$ and $\sigma^{\text{eff}}(\mathbf{r} \in \mathcal{E})$. The initially unknown charge densities of the dielectric and electrode boundaries are the joint solution of these two integral equations.

To solve the integral equations we follow the method of Boda et al. (2006). The surfaces \mathcal{B} and \mathcal{E} are subdivided into curved surface elements. The unknown

charge densities are approximated as uniform within each surface element. The two integral equations then become one system of linear equations in terms of the unknown charge densities of a finite number of surface elements. The accuracy of this approximation is verified by comparing the numerical solution of the discretized integral equations with the analytical result of the integral equations (which is possible for certain geometries) or by verifying Gauss’s theorem for any specific geometry of interest. Examples for the test by Gauss’s theorem are included in Supplementary Materials. This test based on Gauss’s theorem was applied for each specific simulation.

The inhomogeneity of surface charge in our simulation is greatest where point charges of the VS protein are close to a dielectric boundary or electrode. For computational efficiency, we vary the size of the surface subdivisions depending on the distance from the point charges. A typical surface grid (comprising ≈ 6000 surface elements) is shown in Fig. 2 for the dielectric surfaces in the simulation cell. The electrode surfaces (not included in Fig. 2) are subdivided into ≈ 1200 relatively large elements because of their distance from point charges.

The computation of the unknown charges of the surface elements involves solving a linear equation system in terms of as many unknowns (N) as there are surface elements. The coefficient matrix of this system is dense, therefore LU-decomposition time increases with $\mathcal{O}(N^3)$. This computational disadvantage is greatly alleviated by the fact that LU-decomposition of the coefficient matrix needs to be done only once for a given combination of surface geometry and dielectric coefficients. When the S4 charges are moved, solutions to this system of equations are obtained by back-substitution using the same LU-decomposed matrix. That $\mathcal{O}(N^2)$ operation, back-substitution, is required for each sampled configuration of VS charges, but not for each applied voltage tested, as described later.

Computation of charge displacement and electrostatic energy

When the charges of the VS change position, the electric flux toward one bath electrode generally increases by the same amount as the electric flux decreases toward the other bath electrode. To maintain a constant voltage between the two electrodes, charge has to be moved externally between the electrodes. This charge is the experimentally measured displaced gating charge. In principle, one can measure displaced charge in a simulation by monitoring electric flux across a surface surrounding a bath electrode. A more efficient method is provided by the Ramo-Shockley (RS) theorem (Shockley, 1938; Ramo, 1939); for an application to ion channels see (Nonner et al., 2004)). The RS theorem lays the groundwork as well for an efficient method of computing the electrostatic energy of VS configurations when the applied voltage is varied (He, 2001). The RS theorem is applicable to systems containing linear dielectrics.

The RS theorem can be formulated for the configuration of electrode potentials in this study. We apply equal and opposite potentials $V_m/2$ and $-V_m/2$ to the internal and external bath electrodes to create a membrane voltage V_m (defined as internal minus external potential). This method of applying a mem-

brane potential maintains global electroneutrality of the simulation system. We determine the displaced charge in a simulation in two steps:

1. Set all point charges to zero and apply $+1/2$ volt at the internal and $-1/2$ volt at the external bath electrode. Solve for the unknown electrode and induced boundary charges. From the electric potential $V_0(\mathbf{r})$ produced by these charges, an ‘electrical distance’ can be computed as the ratio $[V_0(\mathbf{r})] / [1 \text{ volt}]$ for any geometrical location \mathbf{r} in the simulation cell.
2. For a simulation run with the actual point charges q_k present and actual potentials $V_m/2$ and $-V_m/2$ applied at the electrodes, determine the displaced charge Q_k from the relation:

$$Q_k = q_k \frac{V_0(\mathbf{r}_k)}{1 \text{ volt}} \quad (7)$$

with the electrical distance computed as described in step 1. When several point charges are in the simulation, total displaced charge is the algebraic sum of the displaced charges defined by Eq. 7 for each point charge:

$$Q = \sum_k Q_k \quad (8)$$

Step 1 is executed once for the chosen configuration of electrodes and dielectrics in the simulation (including dielectric coefficients). Step 2 is executed once for each varied configuration (or number) of point charges for which displaced charge is determined. Since the displaced charge determined in step 2 is invariant with respect to the potentials applied at the electrodes, it does not need be re-calculated for the same point-charge configuration when electrode potential is varied.

Note that the electrical distance obtained with the equal and opposite electrode potentials varies between $-1/2$ and $+1/2$ as the point charge is moved from the internal to the external bath electrode. The electrical distance zero corresponds to geometrical locations where the point charge induces equal amounts of charge on either bath electrode.

The RS theorem also makes it possible to compute the electrostatic energy in an efficient two-step procedure (He, 2001):

1. In the full simulation system (including the point charges), impose the potential $V_{\mathcal{E}} = 0$ on all electrodes. Calculate the electrostatic interaction energy W_1 in the system with the point charges q_k at positions \mathbf{r}_k from the relation:

$$W_1 = \frac{1}{2} \sum_k q_k V^{V_{\mathcal{E}}=0}(\mathbf{r}_k) \quad (9)$$

where V is computed with Eq. 4.

2. Calculate the displaced charge Q corresponding to the point charges and their positions using Eq. 8. For the imposed voltage V_m , calculate:

$$W_2 = -QV_m \quad (10)$$

Step 1 of this procedure is executed once for each sampled location of the point charges. Step 2 is executed repeatedly for each applied voltage that is tested. The electrostatic configurational energy in the simulation with the applied voltage V_m is the algebraic sum of the energies calculated in steps 1 and 2:

$$W = \frac{1}{2} \sum_k q_k V^{\varepsilon=0}(\mathbf{r}_k) - QV_m \quad (11)$$

Using the RS theorem in these secondary calculations greatly increases computational efficiency of simulations. This is the basis for our systematic explorations of models.

The calculation of displaced charge and electrostatic energy via Eqs. 8 and 11 are independently verified by computing the electrostatic work through a second route. We alternatively compute the work from the path integral of the electric force acting on the charges q_k of the VS as those charges move from \mathbf{r}'_k to \mathbf{r}''_k :

$$\Delta W = \sum_k q_k \int_{\mathbf{r}'_k}^{\mathbf{r}''_k} \mathbf{E}(\mathbf{r}_k) \cdot d\mathbf{r}_k \quad (12)$$

Here, the electric field is the field of all charges in the system, including the electrode charges provided by the external source that maintains the electrode potentials as VS charges move along their paths. An example of this control (showing consistency) is given in Supplementary Materials (Fig. S2).

Statistical mechanics

Displaced gating charge is experimentally measured from ensembles of channels and thus is an ensemble average. Our electrostatic calculations yield both the displaced charge and the electrostatic part of the configurational energy for a given configuration of a simulated VS model. We consider whole-body movements of S4 charge in two degrees of freedom: translation along the S4 axis and rotation about that axis. Our computational method is efficient enough to allow systematic sampling of this configuration space. We represent each dimension by 51 equally spaced grid nodes and compute the electrostatic energy for the 2601 nodes of the two-dimensional space.

The energy samples define a canonical partition function describing the consequences of the electrostatics on the distribution of an ensemble in the discretized configuration space:

$$\mathcal{Q} = \sum_{i,j} e^{-W_{ij}/k_B T} \quad (13)$$

where i and j are the indices of the rotational and translational discrete positions; W_{ij} is the electrostatic configurational energy of the voltage sensor at translational position i and rotational position j ; k_B is the Boltzmann constant; and $T = 298.15$ K is the absolute temperature. The sampled rotational range is 360° , and a typical translational range is -1.925 nm to $+1.925$ nm relative to

the central position of the S4 charges in α -helical models. Configurations near the ends of the chosen translational range have very small probabilities due to their large electrostatic energy.

The probability of a VS configuration is then:

$$P_{ij} = \frac{1}{Q} e^{-W_{ij}/k_B T} \quad (14)$$

and the expectation value of a random variable X is:

$$\langle X \rangle = \sum_{i,j} X_{ij} P_{ij} = \frac{1}{Q} \sum_{i,j} X_{ij} e^{-W_{ij}/k_B T} \quad (15)$$

One example of a random variable of interest is the charge displaced at an applied voltage. By applying Eq.14, the charge/voltage relation for the model can be predicted for direct comparison with experimental observation of that relation.

We also determine expectation values of random variables over the rotational degree of freedom for a particular translational position i :

$$\langle X_i \rangle = \sum_j X_{ij} P_{ij} = \frac{1}{\sum_j e^{-W_{ij}/k_B T}} \sum_j X_{ij} e^{-W_{ij}/k_B T} \quad (16)$$

The (Helmholtz) free energy of our canonical simulation system is given by the statistical-mechanical relation:

$$A = -kT \ln Q \quad (17)$$

Online Supplemental Materials

Figs. S1 and S2 provide controls for the numerical accuracy in solving the model. One tests the computation of charge induced by the VS charges on the boundary of the protein dielectric and is based on Gauss's law. The other tests the computation of electrostatic energy by an independent method (by integrating force along a given S4 path).

Figs. S3 through S6 and the associated animations (Animations S1–S4 respectively) illustrate VS geometry or movement in four simulations presented in this paper. They show the mean position(s) of VS charges superimposed to the distribution of charge density in the microscopic system. In the animations, voltage is changed in a ramp from -100 to +100 mV.

Results and Discussion

The relation between the displaced gating charge and the applied membrane potential in a sliding-helix model of an individual VS domain is shown in Fig. 3A. The solid line represents the computed relation. Symbols reproduce the relation experimentally observed in *ShakerB* potassium channels (Seoh et al., 1996, Fig. 2A) — the experimental charge per channel was divided by the number of channel monomers, 4. Three observations can be made by comparing the two relations: (1) the total amounts of charge that can be moved by large changes of voltage are similar, ≈ 3 elementary charges per VS domain; (2) the slopes of the two relations are similar, but not equal; (3) a shift along the voltage axis is needed to align the midpoint of the computed relation to the midpoint of the experimental relation (dotted line).

The VS charges in the simulation for Fig. 3A are arranged according to an α -helical geometry (Figs. 2 & S3). An analogous simulation in which the VS charges conform to a 3_{10} -helical geometry (Fig. S4) yields a different result (Fig. 3B). With regard to the experimental charge/voltage relation, the 3_{10} model yields less total charge movement over the tested voltage range and a smaller maximum slope.

The model parameters giving the charge/voltage relation in Fig. 3A are the initial reasonable choices/guesses made in this study as a basis for comparison, except for the spacing of counter-charges which was chosen from three variations made of the α -helical S4 model. The spacing used prevents S4 charges from simultaneously aligning with more than one counter-charge within the average range of travel (Fig. 3, legend). The counter-charges in the 3_{10} -helical model of Fig. 3B were arranged using the same rule of spacing between counter-charges. No attempt is made at this stage to find counter-charge positions giving potentially more realistic charge/voltage relations for the 3_{10} -helical model.

In the following, we use the models of Fig. 3 as ‘standard’ models that are altered to explore sensitivity to variation of physical or geometrical parameters. The primary questions we address are: (1) Which parameters are more (or less) important for gating charge displacement? (2) In which ways are these parameters important for a sliding helix mechanism? Our simulations with varied parameters reveal model designs that predict experimental relations between charge displaced and voltage more closely than does the standard model used for Fig. 3A. However to make comparisons of experimental and simulated relations, at least three caveats need to be considered:

1. Experimental gating charge is measured using a ‘ P/n ’ protocol (Armstrong and Bezanilla, 1977) by which linear charge displacement is eliminated from the record to uncover non-linear charge displacement presumably associated with VS motion. If a P/n protocol measures ‘linear’ charge displacement between voltages at which VS charge displacements are not equal, the protocol eliminates displacement associated with the VS itself (scaled by the factor n). The theoretical charge/voltage relations shown here comprise *all* displaced charge. For an accurate comparison to ex-

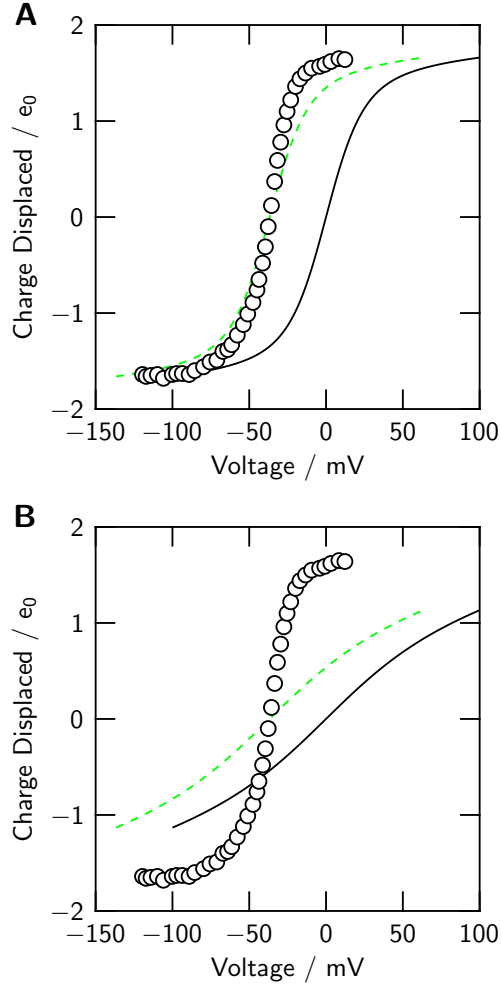


Figure 3: *Theoretical charge/voltage relations compared to experiment.* (A) α -helical S4; (B) 3_{10} -helical S4. Computed relations are shown as solid lines. An experimental relation for *Shaker* K^+ channels (Seoh et al., 1996) is shown as symbols. Dashed lines: computed curves shifted to match the midpoint of the experimental curve. Simulations of the ‘standard’ models are described in section ‘Model and boundary conditions’. The counter-charge spacing is set to $2/3$ of the (translational and rotational) interval of the S4 charges, for both the α - and the 3_{10} -helical S4 models.

periment, these relations would have to be subjected to the specific P/n subtraction procedure used in the experiment. The unsubtracted relations that we present contain the information needed to decide where a P/n subtraction procedure would eliminate actual gating charge (e.g., the simulation results of Fig. 3B).

2. Theoretical charge displacement is associated with a known geometrical position of the VS charges. Experimental charge displacement is not referenced to a known geometrical position. To compare with theory, we assign the experimental charge displacement a reference midway between zero and the charge measured at the largest tested depolarization. In interpreting experiments, that is an arbitrary choice to be made for each version of natural or engineered channel. We represent the simulated charge displacement as relative to the electrical distance 0 as defined in Methods. In the case of the models for Fig. 3, this electrical distance coincides with the geometrical translation $z = 0$ because of the symmetry of the dielectrics.
3. The VS domain in the simulation operates under different conditions from the VS domains in a full channel. The model transduces voltage changes solely into changes of position of the VS. The VS domains integrated into a channel also transduce voltage changes into action on other domains controlling ion flow in the central pore. A shift along the voltage axis (as suggested by Fig. 3) is one possible way in which a ‘load’ may be reflected in the charge/voltage relation of the VS.

The simulations reported in Fig. 3 indicate that voltage sensing by a sliding helix is robust from an engineering point of view. Either the α - or 3_{10} -helical S4 structure can produce voltage-dependent charge displacement, even though the structures lead to distinct configurations of the charges. The two forms of helix generate different voltage sensitivities in the tested models – but neither form produces catastrophic failure.

The simulated VS models we use have been reduced to a simple geometry and to the electrostatic interactions of point charges and linear dielectrics. Since those models can produce more-or-less realistic behavior, important insights into the VS system may be possible by the rigorous analysis of a few crucial components in a reduced model. A reduced model allows physical features to be changed in an orthogonal and systematic manner. The variations presented in this paper all start from the two ‘standard’ models introduced in this section. A key variable for analyzing change is the configurational energy arising from the electrostatics.

Energetics of sliding-helix models

The mobile charges of the VS model are within the electric field of the charges on the electrodes, of the stationary counter-charges, and of the charges induced in the dielectrics. The charges of the S4 helix are modeled as parts of a solid

body. We consider two degrees of freedom of solid-body motion: translation along the S4 axis and rotation about that axis. Energy is computed on a grid composed over this configuration space (Eq. 11). From the electrostatic energy map, a partition function is constructed (Eq. 13), and from the partition function, statistics of random variables (Eq. 15) are predicted. The energy map thus defines the expectations of observables such as the gating charge displacement (Fig. 3). The random variables computed on this basis do not involve approximations based on interpreting energy maps in terms of equilibrium and transition states (Lecar et al., 2003).

Pseudo-color maps of energy in the two dimensions computed for applied voltages of 0 and -100 mV are shown in Fig. 4. The translational and rotational origin corresponds to the central S4 position shown in Fig. 2 for the α -helix. Energy is presented as relative to that at the origin. The symmetry of these models implies that the map for +100 mV (not shown) is a mirror image of the map for -100 mV.

For a membrane potential of 0 mV, the energy maps of both helical models reveal a trough bounded on all sides by regions of substantially higher energy. The energy trough runs in the direction of proportional translation and rotation for the α -helical S4 model, but it runs in the direction of simple translation for the 3_{10} -helical S4 model. The trough in the map of each model follows the counter-charge arrangement — an arrangement chosen for each model to allow periodic interactions during S4 motion of the S4 charges with the counter-charges. In the α -helical model, the S4 charges and counter-charges are aligned on parallel super-helices, whereas in the 3_{10} -helical model the S4 charges and counter-charges follow straight lines parallel to the helical axis. Lowest electrostatic energies of the α -helical S4 trace the path of a screw, whereas energies of the 3_{10} -helical S4 trace the path of a piston.

The regions outside the energy trough for the 3_{10} -helix have energies about three times as large as those of the α -helix. The electrostatic confinement of the 3_{10} -helix is stronger than that of the α -helix. The strength of confinement correlates inversely with the separation of charges in the two geometries. The cluster of S4 charges and counter-charges is more spread out in space in the α -helical than in the 3_{10} -helical geometry due to the angular separations of charges in the α -helical S4.

The electrostatic energy trough tends to anchor the sliding helix in a transmembrane configuration. The S4 charges that dwell in a given configuration in the region of small polarizability are balanced in the model by counter-charges located in that region. This balance is maintained over the range of S4 travel where equivalent amounts of S4 charge and counter-charge overlap in the region of weak dielectric (see Fig. S3 and Animation S1). A second essential element of balance concerns the transit of S4 charges between the less polarizable gating canal region, and the more strongly polarizable vestibule and bath regions. Any energy change associated with the transit of an S4 charge on one side is balanced on the other side by the opposite transit of an S4 charge. On the other hand, the energy trough generated by the electrostatics of the models is too shallow by itself to ensure long-term stability of the S4 configuration. Stabilizing inter-

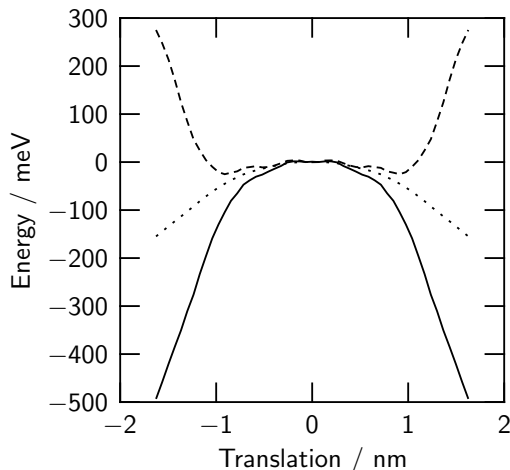


Figure 5: *Energetic consequences of the counter-charges.* Translational energy profile of the α -helical model of Fig. 3A with counter-charges present (dashed line) or deleted (solid line); $\epsilon_p = 4$. The dotted curve is computed with counter-charges deleted and $\epsilon_p = 16$

actions beyond those included in the model (such as interactions provided by the linkers to adjacent transmembrane segments) are most likely necessary for long-term stability.

To inspect the energetics more closely, we construct a one-dimensional energy profile for S4 translation by computing for each translational position the expectation of the electrostatic energy (in the rotational degree of freedom using the rotational partition function, Eq. 16). We refer to this kind of energy profile as a ‘translational energy profile’ for short. Fig. 4E,F show the translational energy profiles for two applied voltages: 0 mV (*solid* lines) and -100 mV (*dashed* lines). The profiles at 0 mV are quite uniform over the translational extent of the energy trough. At a membrane voltage of -100 mV, the energy profiles are tilted in favor of more intracellular positions. A well-defined energy minimum is found at a position about -1 nm inward from the central position of the α -helical S4, whereas a broad minimum spread between -0.7 and -1.2 nm is found with the 3_{10} -helical S4.

The energy profiles in Fig. 4 do not resemble the profile of an ion embedded in a lipid membrane — the latter profile has a high barrier in the center of the weak dielectric (Parsegian, 1969; Neumcke and Lauser, 1969). Instead, in the models the charged section of the S4 helix can travel with an almost level energy over the range of translation where S4 charges overlap with stationary counter-charges. To examine the contribution of the counter-charges to this result, we re-compute the energy profile for the α -helical S4 with the counter-charges deleted from the model (Fig. 5). Deletion of the counter-charges converts the energy trough seen with the standard model (*dashed line*) into a broad barrier (*solid line*). That barrier is reduced but not inverted by increasing the VS

dielectric coefficient ϵ_p from 4 to 16 (*dotted line*). For comparison, a sliding-helix model without counter-charges using $\epsilon_p = 10$ has been analyzed previously by Grabe et al. (2004).

Over the range of translation where the counter-charges produce an energy trough (*long-dashed line*), the deletion of the counter-charges (*solid line*) has a rather small effect (note that we plot energy as relative to the central position). Movement of the S4 helix encounters little energy variation in this region of translation because the amount of S4 charge present in the domain of weak dielectric does not vary: as S4 charge enters on one side, S4 charge leaves on the other side. The energetics are not favorable for these S4 positions (as the charges are not balanced), but they are rather uniformly unfavorable until S4 translation exceeds a distance of about 1 nm from its center position. If the travel of the S4 helix is restricted to ± 1 nm in a biological channel by means other than the counter-charges deleted here, then even an S4 without balancing counter-charges could perform as a voltage sensor.

The variations of energy are small over the traveled range of translation in Fig. 4E,F. The restriction in the model that the S4 domain and its charges must move as a single solid body might be expected to ‘synchronize’ periodic interactions among charges and counter-charges, leading the energetics to express several distinct barriers and wells. The chosen spacing of the counter-charges, however, is enough to prevent the emergence of such a pattern. Additional degrees of freedom are thus not a prerequisite for smooth S4 travel (examples of such degrees of freedom are the possible flexibility of the individual charge-bearing S4 residues or changes in configuration of the helix between the α and 3_{10} forms, Long et al., 2007; Khalili-Araghi et al., 2010; Bjelkmar et al., 2009; Schwaiger et al., 2011),

Although the energy profiles of the two helix forms are similar, the small differences between them are sufficient to produce substantial differences in the relations between charge displacement and voltage (Fig. 3). Simulation results with varied electrostatic parameters presented in the following reveal a number of ways that VS characteristics may be tuned. Because small energy variations control VS behavior, variations in numerous other characteristics of the channel protein might achieve such tuning.

Voltage sensitivity

Hodgkin and Huxley (1952) discovered “the extreme steepness of the relation between ionic conductance and membrane potential”. They attached physical significance to this steepness by supposing that the ion flow is controlled by the distribution of a charged particle that “may rest either on the inside or the outside of the membrane but is present in negligible concentrations elsewhere.” Using Boltzmann’s principle, they derived a relation between conductance and voltage in which steepness is determined by the valency z of the charged particle. The ‘effective valency’ z has been used ever since to empirically quantify the voltage sensitivity expressed in the relations between voltage and ionic conductance, as well as the relations between voltage and displaced gating charge.

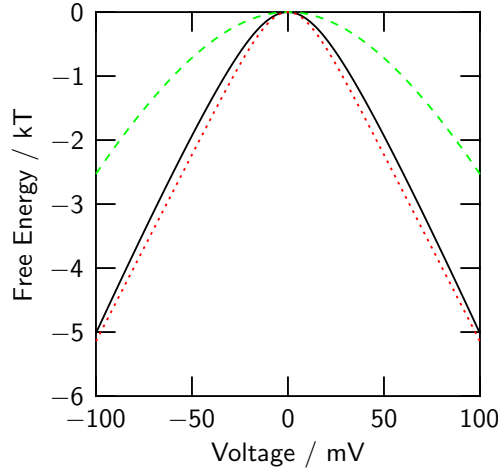


Figure 6: *Voltage dependence of free energy.* Free energy (Eq. 17) for: α -helix model (solid line), 3_{10} -helix model (long-dashed line) and two-state analytic Boltzmann model with $z = 3$ (dotted line). All free energies are relative to the energy at $V = 0$.

The effective valency is model dependent because its physical meaning is defined through the two-state model. The physical meaning of this effective valency is not clear if any other mechanism is at work. Since we study a range of models, a more general definition of voltage sensitivity is needed.

The essence of a voltage sensor is that it derives a change in free energy from an external electrical field, a change which can then drive other processes requiring an increase in free energy in other parts of the channel, such as gating. Therefore to generalize voltage sensitivity, we consider the relation between free energy and applied voltage in our models. Since we simulate a canonical system, the free energy in our case is the Helmholtz energy A as defined by Eq. 17.

Fig. 6 shows the free-energy/voltage relations for our standard α -helical VS model (solid line), our standard 3_{10} -helical model (long-dashed line), and the analytically derived relation for the Hodgkin and Huxley two-state VS model using $z = 3$ (dotted line). The plotted free energies are relative to the free energy applying to $V = 0$. In all cases, increasing the absolute value of the voltage reduces the free energy of the VS system, but the 3_{10} -helical model responds less steeply to voltage than the other models. The α -helical and two-state models produce quite similar changes in free energy.

Applied voltage reduces the free energy of the VS system because states of lower electrostatic energy become available. The free energy does not follow exactly the variation of the expectation of configurational energy (not shown), because the free energy includes both the configurational energy and an entropy term due to the redistribution of the voltage sensor in the configuration space. In microscopic systems like the VS, the entropy contribution to free energy is substantial.

It is important to note that the reduction of free energy with applied voltage

becomes steeper toward voltages where charge displacement (Fig. 3) becomes less steep or saturates. Voltage sensitivity as defined by the slope of the free-energy/voltage relation is then a function over the membrane potential and not just a singular number. This sensitivity is smallest near zero voltage where the charge displaced varies most steeply for these models. Thus the free energy drop due to applied voltage is small where most of the energy received by the VS is used for re-distributing the S4 helix among possible translations. As the re-distribution saturates, free energy approaches a linear relationship with voltage (as does the energy) because the electrical potential at which the S4 charges are located varies linearly with applied voltage. Free energy thus varies the most where charge redistribution is minimal. The asymptotic slopes of the free-energy/voltage relation are determined by the maximal gating charges that can be displaced in either direction from the translation corresponding to electrical position zero.

These observations on free energy/voltage relations show that it is not the movement itself of the S4 helix that produces the free energy picked up by the VS. Actually, the free energy is determined by the increase in the electrical field acting on the S4 charges that have reached nearly saturated positions. Thus the usefulness of the VS ‘muscle’ is chiefly in isometric work or against a workload requiring a large membrane voltage to overcome. The relations shown in Fig. 6 describe the idle VS with no work done on other parts of the channel. The change in free energy due to applied voltage is thus an upper limit for the free energy available to other parts of the channel.

Since the physiological voltage range is smaller than the range simulated in Fig. 6, the ‘sluggish’ redistribution of VS charge of the 3_{10} -helical model causes a severe limitation in the amount of work that can be delivered by this sensor. This limitation occurs despite the fact that the electrostatic energy trough (Fig. 4F) in principle allows a range of S4 play comparable to that in the α -helical model (Fig. 4E). The full work corresponding to the total gating charge that the 3_{10} -helical S4 can produce at extreme voltages cannot be delivered within the physiological voltage range because the gating charge is not rearranged within a narrow interval of voltage.

In the simulation studies that follow, the total charge moved is a more robust property than the swift redistribution of gating charge in response to voltage, which is a property more sensitive to variation in many of our model parameters. Both aspects limiting voltage sensitivity, the total gating charge and the steepness of charge re-distribution, are readily recognized in the experimentally observable charge voltage relation, provided that the experimental charge per VS is determined. Therefore we will discuss parameter variations using charge/voltage relations rather than free-energy/voltage relations.

Polarizability of the protein

The dielectric coefficient ϵ_p assigned to the VS in our models parameterizes the polarizability of a protein, and thus implicitly describes re-adjustments of electrons, atoms and groups of atoms in response to S4 movement. The dielectric

coefficient implies a large number of internal degrees of freedom beyond the two degrees of freedom in whole-body motion sampled explicitly. It is important therefore to determine how much electrical polarization can contribute to shaping VS characteristics. We assess the consequences of polarization for model behavior by varying ϵ_p over a range of values used in other theoretical studies of proteins (reviewed by Schutz and Warshel, 2001) without concerning ourselves with the physics underlying polarization in the VS. Our computations give consistent solutions for a system with piecewise homogeneous linear dielectrics and include appropriate boundary conditions.

A large dielectric coefficient ϵ_p reduces the effective charges of the VS (Eq. 2), the field produced by the effective charges inside the protein (Eq. 3), and thus the charge induced on the protein boundary (Eq. 5). A large ϵ_p weakens the local interactions of S4 charges with counter-charges and induced charges, flattening the energy landscape for S4 movement.

Using the α -helical S4 model of Figs. 3A, 4A,C, the translational energy profiles are computed with varied protein dielectric coefficients ϵ_p (Fig. 7A). The profiles of the dominant energy trough become flatter as ϵ_p is stepwise increased from 2 to 16. Even with $\epsilon_p = 2$, translational energy in the trough varies by no more than 0.05 eV (≈ 2 kT).

As described earlier, moderate variations in energy profile significantly alter the charge/voltage relation (Fig. 7B). The steepness of charge re-arrangement is reduced as ϵ_p is increased. Asymptotic behavior changes from approximately exponential toward hyperbolic.

All simulations for Fig. 7 use the same dielectric geometry, protein charges and counter-charges in the model. Nevertheless, the ‘effective gating charge’ of the VS as assessed by the steepness at the midpoint of the charge/voltage curve increases as the protein dielectric coefficient is reduced. The energetic basis for this effect of the dielectric coefficient is evident in Fig. 7A. With a dielectric coefficient of 2, there are two distinct energy minima at translations of ± 1 nm. With a dielectric coefficient of 16, however, there is very little energy variation among the positions within the energy trough (in the absence of an applied voltage).

The distribution of S4 translational positions varies between two extremes: one, a discrete distribution commonly called a ‘two-state Boltzmann distribution’; the other, a continuous distribution within a space of uniform potential energy. For a graphical representation of these differences in distribution, see the discrete distribution of charge in the Animation S1 with $\epsilon = 4$ and the continuous distribution in Animation S3 with $\epsilon = 16$. For the extremes of the discrete and continuous distributions, the midpoint slopes of charge/voltage curves are analytically known. The midpoint slope of the charge/voltage curve is three times greater for the two-state case than for the uniform-energy case (Neumcke et al., 1978). Thus, the same structural charges produce up to a three-fold varying ‘effective gating charge’ as the protein dielectric coefficient (and therefore the potential energy landscape) is varied. Furthermore, the analytical asymp-

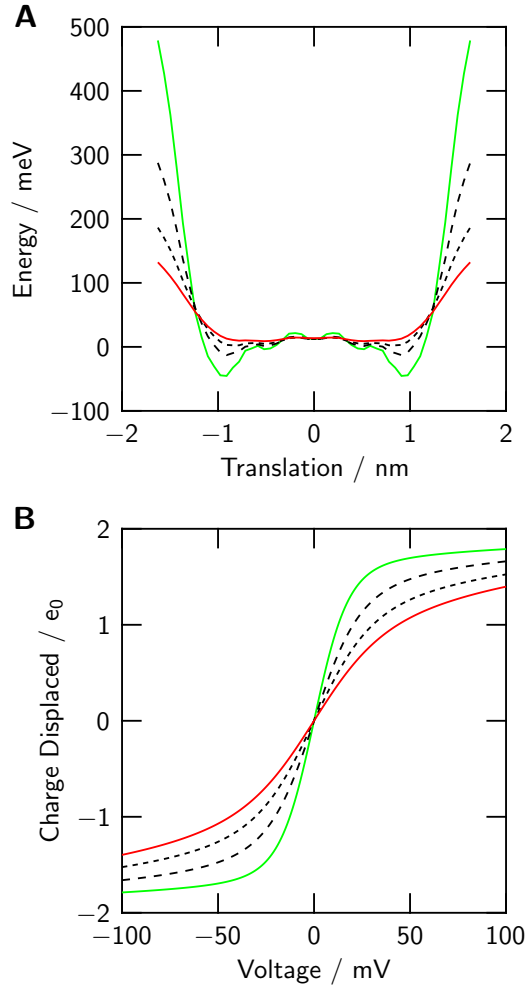


Figure 7: *Effects of protein dielectric coefficient.* The standard α -helical model is solved for 4 different settings of ϵ_p : 2 (solid green line), 4 (short-dashed line), 8 (long-dashed line), and 16 (solid red line). A: translational energy profiles; B: expectation of the charge/voltage relation.

totes are exponential for the two-state energy profile, but hyperbolic in voltage for the flat energy profile.

Published theoretical studies of the VS used $\epsilon_p = 15$ (Lecar et al., 2003) or $\epsilon_p = 10$ (Grabe et al., 2004)). In our simulations, protein dielectric coefficients from 2 to 16 have small effects on the translational energy profile. The profile is dominated by an energy trough that allows for the translation range where the intrinsic counter-charges of the VS overlap with an equivalent number of S4 charges. This trough is in fact deeper for smaller values of ϵ_p than for larger values (Fig. 7A). With charge balance established inside the region of weak dielectric, charges induced on the aqueous boundaries of the dielectric are small and their interaction with S4 charges does not dominate the translational energy profile.

In a 3_{10} -helical model using $\epsilon_p = 4$ (Figs. 3B and 4F), a slightly V-shaped energy profile produces an even smaller voltage sensitivity than that seen in the α -helical model using $\epsilon_p = 16$ (Fig. 7B). The 3_{10} -helical model in the presented form has difficulty producing steep charge/voltage relations like those observed in biological channels. On the other hand, the energetic differences determining slope are small, so that the seemingly unfavorable characteristics of the 3_{10} -helical S4 might be overcome in numerous ways in biological channels.

The simulations with varied polarizability also give information regarding the physical origin of the energy minima seen at the ends of the range of travel of the α -helical model and the small upward step in electrostatic energy seen in these positions for the 3_{10} -helical model. It is important to note that the shown energy profiles are relative to those in the center position of these helices – these are not the absolute energies associated with assembling the system (which are not shown). In absolute terms, electrostatic energies increase as protein dielectric coefficient is reduced. The energy wells seen in profiles associated with small polarizability reflect a smaller increase of electrostatic energy in some positions. These wells (and the upward steps found near the ends of the energy trough for the 3_{10} -helical model, Fig. 4F) are a collective result of the entire charge cluster in the VS interacting with induced charge on the protein boundary. The more dense cluster of the 3_{10} -helical model has stronger interactions among charges and counter-charges, and with the charges induced on the protein dielectric, than does the more spread-out (in the angular dimension) cluster of charges in the α -helical model. The difference is strongest in the extreme allowed positions of S4 travel, when a maximal number of S4 charges is located in either one of the aqueous phases near the protein boundary.

These simulations with varied dielectric coefficient thus lead us to conclude that protein polarizability is not crucial for electrostatic stability of a sliding-helix VS that balances S4 charges by counter-charges. On the other hand, the degree of polarizability contributes to determining the relation between voltage and displaced charge.

Geometry of the gating canal

About 10 residues of the S4 helix are inaccessible to hydrophilic reagents applied to resting channels from either the extracellular or intracellular side (Gandhi and Isacoff, 2002). If the S4 domain is α -helical and oriented perpendicular to the membrane plane, then the inaccessible translational range is only ≈ 1.35 nm long and thus shorter than the lipid core of the membrane. Therefore the S4 helix is thought to move across the hydrophobic region in a short ‘gating canal’ that forms an electrical seal between water pockets extending toward the canal from either side (vestibules). One consequence of this arrangement is that most of the applied electrical voltage drops over a short length of the gating canal and is thereby ‘focused’ on the interval of S4 charges dwelling in the canal itself.

Short of a simulation, approximate inferences can be made of potential electrostatic consequences of the gating canal. If the queue of S4 charges spans the gating canal plus the range of S4 travel, then the instantaneous force F exerted by the applied field on the n S4 charges simultaneously present in the canal of length D is approximately $F = ne_0V_m/D$. The length D and the number n are related by the axial spacing of the charges in the S4 helix: $d = D/n$ (assuming that ‘in the canal’ on average implies an extra distance at either end of about $d/2$). The electrical force acting on the S4 charges is thus $F = e_0V_m/d$. Therefore this force F is independent of the length of the gating canal, depending only on the spacing between S4 charges. The instantaneous work done by the field on the S4 charges as the S4 moves through the canal is given by $W = Fmd = me_0V_m$, where m is the number of S4 charges that travel across one of the gating canal mouths during the motion associated with the work W . This work does not depend on the length of the gating canal. Moreover, the S4 charges travel the same distance md per unit work regardless of the length of the gating canal, D . Voltage sensitivity (defined by force or work picked up per unit applied voltage) does not depend on the focusing of the electric field by the gating canal itself, as long as the queue of S4 charges extends across the gating canal.

To assess more fully the consequences of gating canal geometry, we simulate varied canal lengths and/or canal positions with respect to the membrane planes in the VS model (Fig. 8). Starting with the geometry of our standard model for the α -helical VS (VS protein outline 1, compare Fig. 1), we shift the canal toward the intracellular membrane plane (outline 2). Two further variations include a reduction of the vestibule length on both sides by one half, thereby lengthening the gating canal (outline 3) and a shift of that lengthened gating canal (outline 4, Fig. S6).

With both the centered and the shifted gating canals, lengthening the canal increases the slope of the charge/voltage relation while maintaining the maximal charge displacement between ± 100 mV (Fig. 8A, line patterns in the graph correspond with the protein outlines below the graph). Shifting the position of the gating canal shifts the charge/voltage relation along both the voltage axis and the charge axis (towards the intracellular side) while maintaining the slope typical of the canal length. These shifts indicate that asymmetries of the

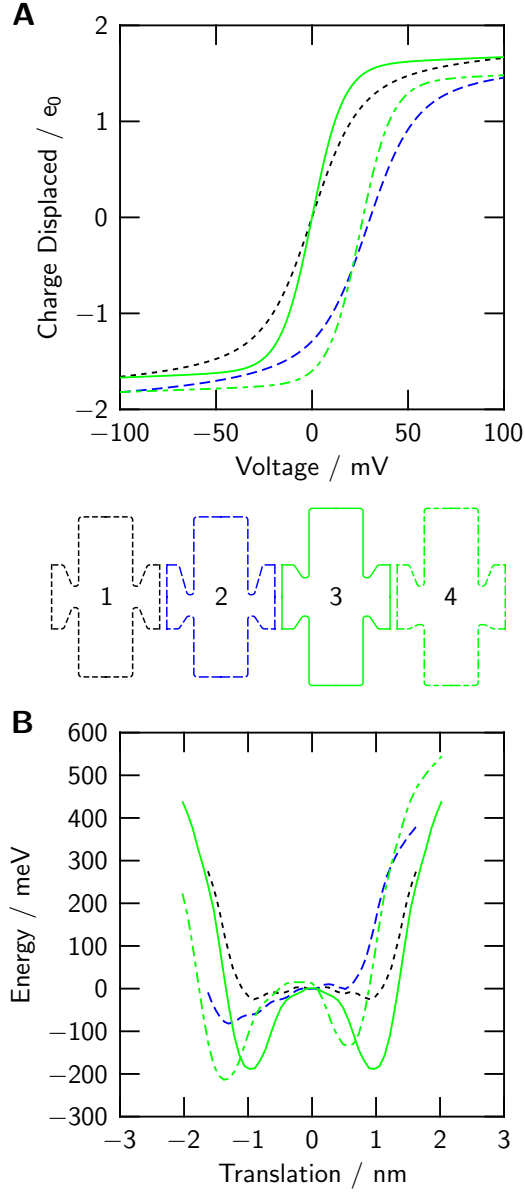


Figure 8: *Consequences of gating pore geometry.* Length and/or position of the gating canal (and hence its vestibules) are varied as shown by the outlines of the VS protein between the graphs. Outline 1 is our standard α -helical S4 model. The line patterns & colors in both the graphs of the charge/voltage relations (A) and the underlying translational energy profiles (B) correspond to the line patterns & colors used for the outlines of the VS shapes. Table 1 gives further geometrical specifications for shapes 1–4. Outline 4 can be seen in the 3-dimensional Fig. S6.

vestibules of the gating canal bias the voltage sensed by the S4 segment.

The underlying energetics are summarized in Fig. 8B. Lengthening the gating canal increases the depth of the energy minima at the ends of the range of travel, thus promoting the bistable behavior of the VS associated with a steep slope of the charge/voltage relation. Shifting the position of the gating pore shifts the energy profile and therefore the S4 geometrical range of travel. The translational spacing between the minima at either end of the energy trough is not changed by these variations of gating canal geometry.

The observed invariance of the total charge displaced in these simulations conforms to our earlier approximation ($W = me_0V_m$). Geometrical S4 travel relative to the center of the membrane tends to follow the position of the gating canal. A longer gating canal giving *less* ‘focusing’ of the applied electric field results in a *steeper* charge/voltage relation. The latter two relations are due to the self-energy contribution to the configurational energy as defined by Eq. 9, that is to the electric field when $V_m = 0$ is applied to the bath electrodes. In this section’s simulations, the counter-charges to the S4 charges are aligned to the center of the septum of the gating canal which, when the gating canal is shifted, varies from the center of the membrane and the S4 protein region. The counter-charges’ mutual spacing continues to be constant. With a longer canal, there is a longer gap between the outermost counter-charge and the central end of the vestibule on each side. The energy minima of the translational energy profile are located at the S4 translational coordinate associated with the trailing charge of the S4 helix vacating the poorly screened stretch of the gating canal (see Animation S4 for associated charge distributions).

Screening of VS charge exposed to the aqueous solutions

Translocation of S4 charge across the membrane necessarily shifts a high local density of protein charge across the membrane. Therefore the energetics of S4 translation should depend on the screening on either side of the membrane of S4 charges by bath ions. We have thus far reported on VS models under symmetrical screening conditions; under those conditions, any screening effects on S4 energetics are masked by mutual compensation. Strongly asymmetrical screening should unmask the contribution of screening to the energetics. Our simulation does not include explicit bath ions, as we explore screening effects instead by varying the distance of the bath electrodes from the membrane and VS protein surfaces (see section ‘Model and boundary conditions’). The two extreme electrode placements shown in Fig. 1A,C are equivalent to low millimolar ionic strength baths and exceedingly large ionic strength baths.

We compute the charge/voltage relations for our standard α -helical model with three electrode configurations (Fig. 9A): (1) both electrodes far from the membrane and protein, (2) both electrodes directly on the surface of the membrane and protein, and (3) the external electrode on the membrane and protein, and the internal electrode far from the membrane and protein. The charge/voltage relation for configuration 2 (solid line) reveals a larger total displaced charge and a steeper slope compared with configuration 1 (dotted

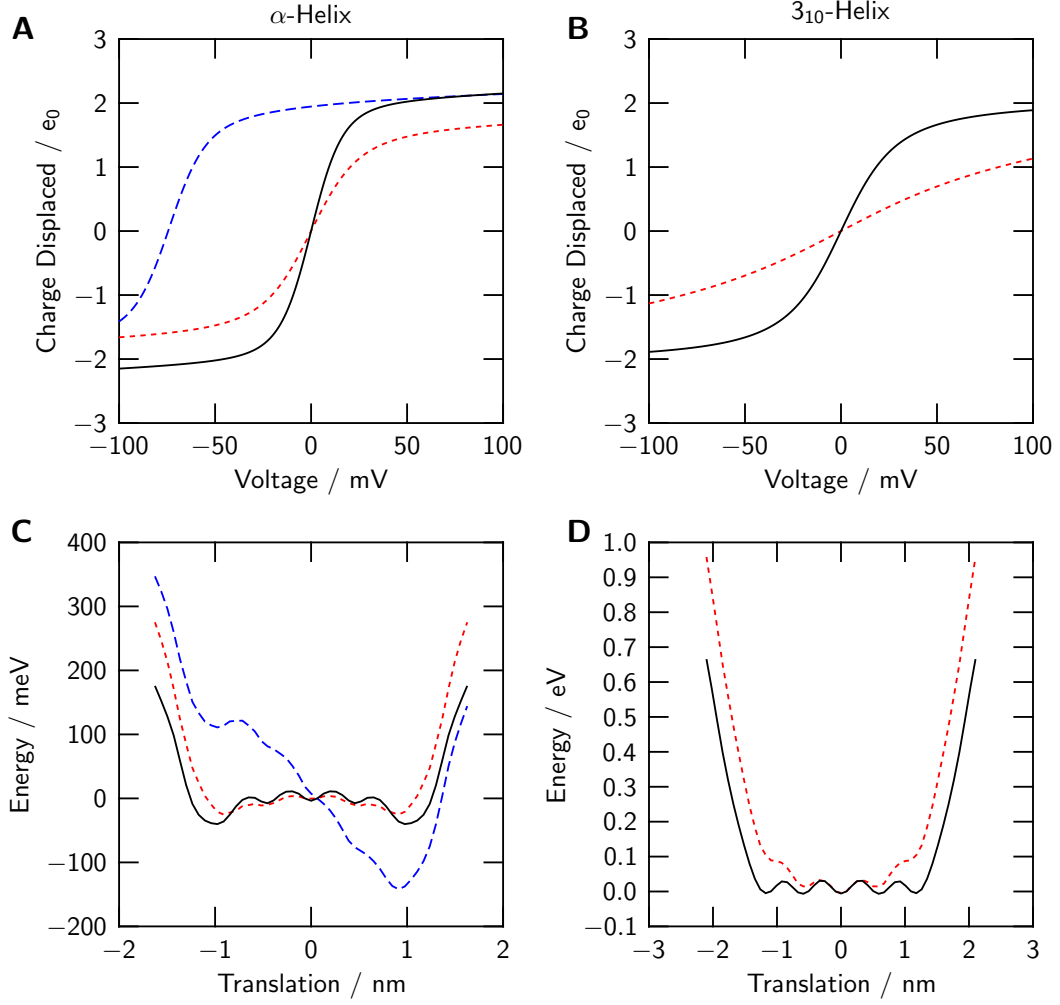


Figure 9: *Consequences of screening by the baths.* (A, C) The standard α -helical S4 model is simulated with varied electrode arrangements to mimic varied ionic strength of the baths (see Fig. 1). Charge/voltage relations and translational energy profiles correspond to symmetrical low ionic strengths (short-dashed lines, geometry as in Fig. 1A), symmetrical high ionic strengths (solid lines, geometry as in Fig. 1C), and external low and internal high ionic strengths (long-dashed line, geometry as in Fig. 1B). (B, D) Analogous simulations of the 3_{10} -helical S4 model for symmetrical low or high ionic strengths.

line). This increase in total charge at ‘high ionic strength’ has two sources: the increase in electric distance between geometrical S4 positions (as discussed by Islas and Sigworth, 2001); and the increase in the S4 geometrical range of motion at ± 100 mV, as indicated by the energy minima of translational energy profiles (Fig. 9C). The increase in slope is due to the deeper translational energy minima at the extreme positions, which promote bistable behavior as described earlier.

The simulation for configuration 3 (low internal and high external ionic strength) yields a left-shifted charge/voltage relation (long-dashed line in Fig. 9A). The magnitude of this shift is due to the asymmetrical screening of S4 charges on the internal and external sides; the S4 charges are attracted toward the external bath where screening is more effective. This result shows that the screening of bath-exposed S4 charges contributes substantially to the energetics of S4 translation. This contribution is masked by mutual compensation when ionic strengths are equal on both sides, except for contributions in terms of more subtle variation of the shape of the charge/voltage relation.

The 3_{10} -helical model gives substantially smaller voltage sensitivity than the α -helical model when we simulate the models with ‘low ionic strength’ electrode placement. Given the effects of screening on voltage sensitivity seen in Fig. 9A, it is interesting to see to what extent strong screening ‘rescues’ voltage sensitivity of the 3_{10} -helical model. In fact, exceedingly large ionic strength increases voltage sensitivity substantially (solid line in Fig. 9B) in terms of both increased maximum slope and total charge displaced across the simulated potential. However, this ‘rescue’ does not push voltage sensitivity all the way to that found for the α -helical model (solid line in Fig. 9A). The corresponding translational energy profiles for the 3_{10} -helical model are shown in Fig. 9D.

Islas and Sigworth (2001) found small voltage shifts (< 10 mV) when studying the effects of intracellular variation of ionic strength on charge/voltage relations of *Shaker* channels. They interpreted these observations in terms of the Guy-Chapman theory of the electrical double layer. In those terms, those small shifts indicate a low density of membrane surface charge. In our simulations (Fig. 9A), a unilateral variation of screening causes a large shift even though the model does not include surface charge. Screening of S4 charges by a bath of low ionic strength reduces the electrostatic energy less than the screening of such S4 charges by a bath of high ionic strength. This effect does not require fixed surface charges, but arises from the S4 charges themselves. In contrast to the interpretation given by Islas and Sigworth (2001), the absence of a voltage shift may indicate that fixed negative charge exists at the intracellular end of the gating canal, but that such charge is largely neutralized by the positive S4 charges exposed to the intracellular baths at the midpoint of the S4’s range of travel. The S4 charge exposed in this configuration is then screened by the negative fixed charge regardless of the ionic strength of the bath.

Consequences of ‘surface charge’

The existence of ‘surface charge’ acting on the VS was inferred by Frankenhaeuser and Hodgkin (1957) and many subsequent studies (Hille, 2001). Negative charges on residues of the extracellular loop connecting the S5 and pore segments of Kv channels determine the voltage for activating the channel (Elinder et al., 1998; Elinder and Århem, 1999). One residue is conserved in that region – E418 for *ShakerB* – while others are variable. E418 is involved in mediating activation-related slow inactivation and has been proposed to interact at close range with the outermost S4 charge (R362) when the VS is in the activating position (Larsson and Elinder, 2000; Elinder et al., 2001).

We model surface charge as discrete by placing a point charge of $-e_0$ into either one bath at translation 1 nm or both baths at ± 1 nm, which are the translations approached by the terminal S4 charges at voltages of ± 100 mV. The charge is given the same radial distance from the S4 axis as the counter-charges located inside the protein. Two angular positions are tested: a ‘close’ one aligned with the terminal S4 charge, and a ‘far’ one turned 180° away from the S4 charge.

The charge/voltage relations for our standard α -helical S4 model with four surface charge arrangements added are shown in Fig. 10A: one external charge in the far position (*short-dash line*); one external and one internal surface charge, with both in the far positions (*dotted line*); one external charge in the close position (*long-dash line*); and one external and one internal charge, with both in the close positions (*solid line*). The far external charge shifts the charge/voltage relation, producing the signature of a surface charge. The combination of far external and far internal surface charges slightly reduces the slope of the charge/voltage relation with respect to the model without surface charges (compare Fig. 3). The combination of close internal and close external charge also produces no shift (due to symmetry) but does steepen the slope of the charge/voltage curve (compare Fig. 3A). With only the close external charge, the charge/voltage relation is shifted, and at negative voltage, the asymptote is slightly less steep relative to the asymptote with both surface charges. Thus surface charges have position-dependent effects on both the midpoint and slope of charge/voltage relations.

Elinder et al. (2001) estimated the contributions of individual surface charges present in K^+ channels to voltage shift in charge/voltage relations, using the voltage shifts of ionic conductance observed with varied Mg^{2+} concentrations. Our simulated shifts are in the range of those estimated shifts. Elinder et al. (2001) interpreted the varied shifts estimated for different charged residues to be a consequence of the distance from the VS charges to the charged residues. Our self-consistent simulations with a ‘close’ and a ‘far’ surface charge show only a small effect on voltage shifts due to the distance to the surface charge (long- and short-dashed lines in Fig. 10).

The translational energy profiles from those four surface-charge simulations are shown in Fig. 10B. Far external surface charge chiefly tilts the profile (*short-dash line*), whereas far surface charges on both sides remove the energy wells

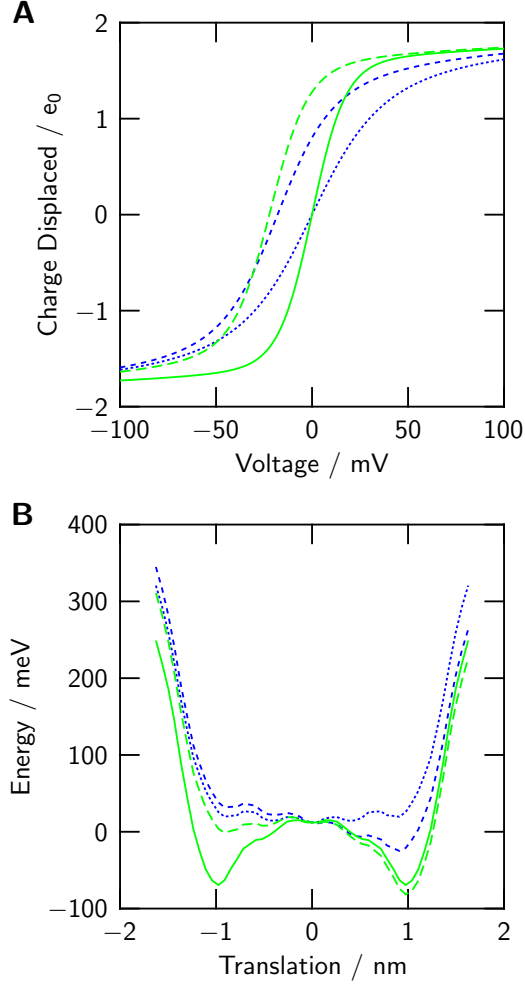


Figure 10: *Consequences of 'surface charge'*. Standard α -helical S4 model with discrete surface charge(s) added in three variations of geometrical position (detailed in text): close external *and* internal surface charges (*solid line*); close external-only surface charge (*long-dashed line*); far external *and* internal surface charges (*dotted line*); far external-only surface charge (*short-dashed line*). (A) Statistical-mechanical expectations of charge/voltage relations; (B) Translational energy profiles.

near the ends of the energy trough. Close external and internal charges, however, create deeper energy wells at either end of the range of S4 motion (*solid line*). With only a close external charge, an energy well is added at the external end of the range of S4 motion, while energy at the intracellular end of the range is raised (*long-dash line*). The energy well resulting from close interaction with a surface charge increases the electrostatic contribution to S4 transmembrane stability as well, since it lowers the electrostatic energy of that S4 position relative to more extreme S4 positions. This does not occur when the interaction with the surface charge is far.

Conclusion

The sliding helix configuration has an innate electrostatic stability if the helix charges not exposed to water are balanced by fixed counter-charges. This balance extends over the range of helix movement where from about 3 to about 4 charge equivalents are displaced across the membrane field. The limited range of motion at the extremes of physiological membrane potential leads to robustness of VS behavior over a range of conditions and geometrical variations. Whether the geometry is α -helical, 3_{10} helical, in high ionic concentration or low, this basic structural issue leads to a system that results in gating-charge displacement in response to change in transmembrane potential.

On the other hand between those extremes, the energy landscape for a given membrane potential varies between models: from almost flat to two energy troughs separated by a large barrier. Those variations lead to distinct charge displacement patterns (implying distinct kinetics not investigated here). Protein dielectric, gating canal geometry, helix configuration and surface charges alter the behavior of the system, ranging from systems that can be approximated by two-state Boltzmann models all the way to continuous model systems. This results in a family of voltage-sensors with easily perturbed voltage sensitivity despite their robust behavior at their limits. Features not made explicit in our models will likely play a role in that region of sensitivity.

These results suggest a problem with the 3_{10} -helical S4 structure: in the parameter space we studied, the 3_{10} models tend towards poor voltage-sensitivity in contrast with α -helical models which show both higher voltage-sensitivity and greater variation in voltage-sensitivity.

Our simulations exploring the consequences of a set of physical parameters elucidate the electrostatic principles underlying both the robustness of voltage-sensor charge-displacement response and the sensitivity of voltage-sensitivity and gating charge voltage shift in the face of small model variations. Resolving the ‘inverse’ problem of connecting specific experimental data with the specific underlying physics is both a computational and experimental challenge. We suggest that more ‘forward’ simulations of the consequences of physical parameters are needed to guide the design and interpretation of experiments intended to determine fine control of voltage sensing.

Acknowledgments

The authors are grateful for the support of the National Institutes of Health (grant GM083161) to W. Nonner and a Graduate Research Fellowship of the National Science Foundation to A. Peyser. We thank Drs. Alice Holohean, Peter Larsson, and Karl Magleby for helpful discussions.

References

- Armstrong, C. M. and F. Bezanilla. 1977. Inactivation of the sodium channel. II. Gating current experiments. *J Gen Physiol*, 70(5):567–590. URL <http://www.ncbi.nlm.nih.gov/pmc/articles/PMC2228472>.
- Bjerkmar, P., P. S. Niemelä, I. Vattulainen, and E. Lindahl. 2009. Conformational changes and slow dynamics through microsecond polarized atomistic molecular simulation of an integral Kv1.2 ion channel. *PLoS Comput Biol*, 5(2):e1000289. doi: 10.1371/journal.pcbi.1000289.
- Boda, D., M. Valiskó, B. Eisenberg, W. Nonner, D. Henderson, and D. Gillespie. 2006. The effect of protein dielectric coefficient on the ionic selectivity of a calcium channel. *J Chem Phys*, 125(3):34901. doi: 10.1063/1.2212423.
- Catterall, W. A. 2010. Ion channel voltage sensors: Structure, function, and pathophysiology. *Neuron*, 67(6):915–928. ISSN 0896-6273. doi: 10.1016/j.neuron.2010.08.021.
- Elinder, F., Y. Liu, and P. Arhem. 1998. Divalent cation effects on the Shaker K channel suggest a pentapeptide sequence as determinant of functional surface charge density. *J Membr Biol*, 165(2):183–189. doi: 10.1007/s002329900432.
- Elinder, F., R. Männikkö, and H. P. Larsson. 2001. S4 charges move close to residues in the pore domain during activation in a K channel. *J Gen Physiol*, 118(1):1–10. doi: 0.1085/jgp.118.1.1-a.
- Elinder, F. and P. Århem. 1999. Role of individual surface charges of voltage-gated K channels. *Biophys J*, 77(3):1358–1362. doi: 10.1016/S0006-3495(99)76984-5.
- Frankenhaeuser, B. and A. L. Hodgkin. 1957. The action of calcium on the electrical properties of squid axons. *J Physiol*, 137(2):218–244. URL <http://www.ncbi.nlm.nih.gov/pmc/articles/PMC1362975>.
- Gandhi, C. S. and E. Y. Isacoff. 2002. Molecular models of voltage sensing. *J Gen Physiol*, 120:455–463. doi: 10.1085/jgp.20028678.
- Grabe, M., H. Lecar, Y. N. Jan, and L. Y. Jan. 2004. A quantitative assessment of models for voltage-dependent gating of ion channels. *Proc Natl Acad Sci U S A*, 101(51):17640–17645. doi: 10.1073/pnas.0408116101.
- He, Z. 2001. Review of the Shockley-Ramo theorem and its application in semiconductor gamma-ray detectors. *Nucl Instr Meth A*, 463(1–2):250–267. ISSN 0168-9002. doi: 10.1016/S0168-9002(01)00223-6.
- Hille, B. 2001. Ion Channels of Excitable Membranes. 3rd edition. Sinauer Associates, Inc., Sunderland, Mass. USA. 814 pp.

- Hodgkin, A. and A. Huxley. 1952. A quantitative description of membrane current and its application to conduction and excitation in nerve. *J Physiol*, 117(4):500–544. ISSN 00223751. URL <http://http://www.ncbi.nlm.nih.gov/pmc/articles/PMC1392413>.
- Islas, L. D. and F. J. Sigworth. 2001. Electrostatics and the gating pore of *Shaker* potassium channels. *J Gen Physiol*, 117(1):69–90. doi: 10.1085/jgp.117.1.69.
- Khalili-Araghi, F., V. Jogini, V. Yarov-Yarovoy, E. Tajkhorshid, B. Roux, and K. Schulten. 2010. Calculation of the gating charge for the Kv1.2 voltage-activated potassium channel. *Biophys J*, 98(10):2189–2198. doi: 10.1016/j.bpj.2010.02.056.
- Larsson, H. P. and F. Elinder. 2000. A conserved glutamate is important for slow inactivation in K^+ channels. *Neuron*, 27(3):573–583. doi: 10.1016/S0896-6273(00)00067-2.
- Lecar, H., H. P. Larsson, and M. Grabe. 2003. Electrostatic model of S4 motion in voltage-gated ion channels. *Biophys J*, 85(5):2854–2864. doi: 10.1016/S0006-3495(03)74708-0.
- Long, S. B., X. Tao, E. B. Campbell, and R. MacKinnon. 2007. Atomic structure of a voltage-dependent K^+ channel in a lipid membrane-like environment. *Nature*, 450(7168):376–382. doi: 10.1038/nature06265.
- Neumcke, B. and P. Läuger. 1969. Nonlinear electrical effects in lipid bilayer membranes. II. Integration of the generalized Nernst-Planck equations. *Biophys J*, 9(9):1160–1170. doi: 10.1016/S0006-3495(69)86443-X.
- Neumcke, B., W. Nonner, and R. Stämpfli. 1978. Gating currents in excitable membranes. *International Review of Biochemistry, Biochemistry of Cell Walls and Membranes II*, 19:129–155.
- Nonner, W., A. Peyser, D. Gillespie, and B. Eisenberg. 2004. Relating microscopic charge movement to macroscopic currents: The Ramo-Shockley theorem applied to ion channels. *Biophys J*, 87(6):3716–3722. doi: 10.1529/biophysj.104.047548.
- Papazian, D. M., X. M. Shao, S. A. Seoh, A. F. Mock, Y. Huang, and D. H. Wainstock. 1995. Electrostatic interactions of S4 voltage sensor in *Shaker* K^+ channel. *Neuron*, 14(6):1293–1301. doi: 10.1016/0896-6273(95)90276-7.
- Parsegian, A. 1969. Energy of an ion crossing a low dielectric membrane: Solutions to four relevant electrostatic problems. *Nature*, 221(183):844–846. doi: 10.1038/221844a0.
- Ramo, S. 1939. Currents induced by electron motion. *Proc IRE*, 27:584–585. ISSN 0096-8390. doi: 10.1109/JRPROC.1939.228757.

- Schutz, C. N. and A. Warshel. 2001. What are the dielectric “constants” of proteins and how to validate electrostatic models? *Proteins*, 44(4):400–417. doi: 10.1002/prot.1106.
- Schwaiger, C. S., P. Bjelkmar, B. Hess, and E. Lindahl. 2011. 3_{10} -helix conformation facilitates the transition of a voltage sensor S4 segment toward the down state. *Biophys J*, 100(6):1446–1454. doi: 10.1016/j.bpj.2011.02.003.
- Seoh, S.-A., D. Sigg, D. M. Papazian, and F. Bezanilla. 1996. Voltage-sensing residues in the S2 and S4 segments of the *Shaker* K^+ channel. *Neuron*, 16(6):1159–1167. ISSN 0896-6273. doi: 10.1016/S0896-6273(00)80142-7.
- Shockley, W. 1938. Currents to conductors induced by a moving point charge. *J Appl Phys*, 9(10):635–636. ISSN 00218979. doi: 10.1063/1.1710367.

Supplementary Materials

Tests of numerical accuracy in solving the electrostatics.

The divergence theorem (Gauss’s theorem) states that

$$\oint_S \epsilon(\mathbf{r}) \epsilon_0 \mathbf{E}(\mathbf{r}) \cdot \mathbf{n}(\mathbf{r}) \, da = \int_V \rho^{\text{src}}(\mathbf{r}) \, d\tau \quad (\text{S1})$$

where S is the closed surface around the volume V , da is the area of the surface element located at $\mathbf{r} \in S$, and $d\tau$ is the volume of the space element located at $\mathbf{r} \in V$. This holds for any geometry of V .

A relevant surface for applying Gauss’s theorem is the dielectric boundary of the VS protein since the electric field at that boundary generates the most important induced charge to be computed. The surface integral in Eq. S1 must yield the algebraic sum of the formal charges that are assigned to the VS residues. Our numerical method approximates the normal field strength (and hence induced charge density) at the surface as piecewise uniform. Gauss’s theorem provides a test in the actual system that we simulate of the accuracy of the induced charge computed on the boundary. The difference between the computed total induced charge Q_{calc} and the charge Q_{Gauss} predicted from Gauss’s theorem is:

$$Q_{\text{calc}} - Q_{\text{Gauss}} = - \sum_j \frac{\epsilon_p \epsilon_j}{\epsilon_j - \epsilon_p} \sigma^{\text{ind}} a_j - \sum_k q_k^{\text{src}} \quad (\text{S2})$$

where a_j is the area of protein surface element j and ϵ_j is the dielectric coefficient on the out-facing side of a_j .

The error in the computed charge calculation is likely to vary as S4 charges are moved in a simulation since the distances between the S4 charges and the dielectric boundaries vary. Fig. S1 shows the error in induced charge calculation for the full range of S4 translational positions in a typical simulation. The error is $\leq 0.008 e_0$ of the actual net charge of $3 e_0$ assigned to the VS in this simulation. The results of our charge calculation are thus in good agreement with Gauss’s theorem, as they must be.

In a second control, we compare the calculations of electrostatic energy by two independent approaches: (1) direct calculation of the energy, using the Ramo-Shockley theorem as described in Methods as our standard procedure; and (2) path-integration of the force acting on the S4 segment via Eq. 12. Both methods use the induced charges on dielectric boundaries and electrodes computed in our simulation and tested using Gauss’s law as described above. Method (1) is based on the potentials produced by all charges. Method (2) is based on the electrical fields of all charges. These methods have no computational overlap following the charge computation (in other words, these methods use distinct code paths, a test for coding correctness). We show this control for three applied voltages with a prescribed (diagonal) path through the translational and rotational dimensions of the range of S4 motion which we typically examine. Fig. S2 shows the energies from Method (1) as dots superimposed on the energies from method (2) as lines.

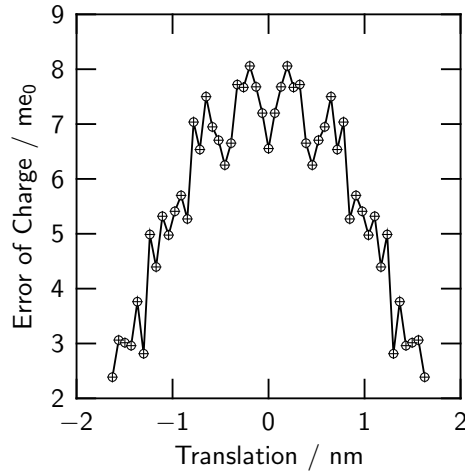


Figure S1: *Test of numerical accuracy using Gauss's theorem.* The difference $Q_{\text{calc}} - Q_{\text{Gauss}}$ as defined by Eq. S2 is plotted versus S4 translation (Eq. 16 is applied to calculate the expectation value over the rotational degree of freedom). Normal electric flux is integrated over the surface of the protein (brown region in Fig. 1). The protein region contains a net charge of $+3 e_0$ (6 positive S4 charges and 3 negative counter-charges), which is recovered from the integrated electrical flux within a relative error of <0.003 over the full range of S4 translation ($\leq 0.008 e_0$). Charge errors computed for three applied voltages (-100 mV, circles; 0 mV, line; 100 mV, crosses) are superimposed in the graph, showing no detectable effect of the external field on the error.

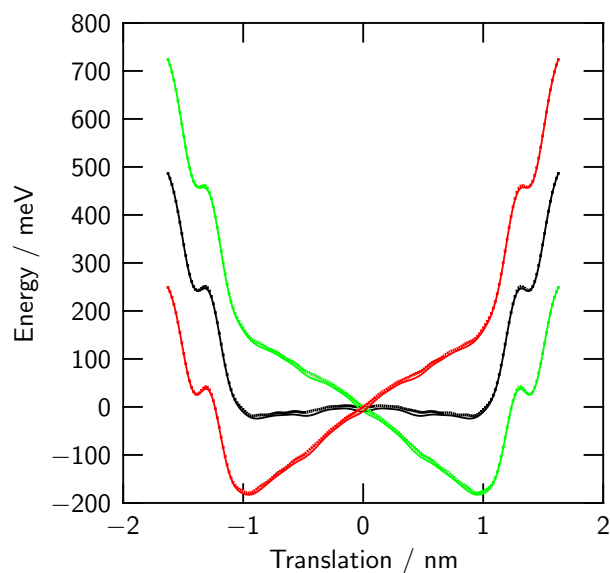


Figure S2: *Control for the computation of energy.* Energy profiles for the fixed path prescribed by the translations plotted as abscissa and the proportional rotational increments such that the standard α -helical model S4 charges follow the curve of counter-charges (from -180 to +180 degrees). Energies computed by integrating the force along this path (lines) are compared with energies computed using the Ramo-Shockley theorem (dots) as described as our routine method in Methods. These tests are applied for three membrane voltages (100 mV, red; 0 mV, black; +100 mV, green). The energies obtained by these two methods are aligned at the most negative translation tested.

Charge distributions of VS models

The sliding helix in our VS models is a microscopic voltage sensor, thus subject to thermal agitation. Its behavior must be described in statistical terms. In this section, stochastic VS behavior is visualized for several models presented in the paper, both as figures for a fixed applied voltage (-100 mV; Figs. S3–S6) and in animations with voltage increasing uniformly over time from -100 to +100 mV (Animations S1–S4, respectively).

The figures show two stochastic aspects of VS behavior: (1) the mean positions of the S4 charges (marked by blue balls), and (2) the charge density distribution of S4 charge (represented by a blue cloud with a color intensity proportional to the charge density there). A high density of color marks the locations where the S4 charges dwell frequently, as opposed to their mean positions.

The mean position for each charge is computed from Eq. 15 using the positions \mathbf{r}_k for the charge q_k as the random variable X , using the partition function with translational and rotational degrees of freedom. Since the helix behaves as a solid body, the helix position \mathbf{r} fixes the positions \mathbf{r}_k for the charges q_k . That relationship allows us to define the partition function for the positions \mathbf{r}_k in terms of the partition function for the helix position \mathbf{r} , as well as the energy functions for \mathbf{r}_k in terms of the energy function for the helix position.

In other words, by applying Eq. 15 to a model with $X = \mathbf{r}_k$, the mean position $\langle \mathbf{r}_k \rangle$ for any charge can be calculated given the probability of configuration ij (P_{ij} , Eqs. 14 & 13):

$$\langle \mathbf{r}_k \rangle = \sum_{i,j} \mathbf{r}_{ijk} P_{ij} = \frac{1}{Q} \sum_{i,j} \mathbf{r}_{ijk} e^{-W_{ij}/k_B T} \quad (\text{S3})$$

where W_{ij} is the work to construct configuration ij and \mathbf{r}_{ijk} is the position of charge k in configuration ij .

Likewise, the distribution of charge can be computed by applying the partition and energy functions in terms of the position of charges \mathbf{r}_k . The charge density $\bar{z}(\mathbf{r})$ is then the sum over all charges of the probability of each charge being located at \mathbf{r} , multiplied by its valency, and normalized:

$$\bar{z}(\mathbf{r}) = \frac{1}{\sum_{i,j,k} P_{ij} z_k} \sum_{i,j,k} P_{ij} z_k \delta(\mathbf{r}, \mathbf{r}_{ijk}) \quad (\text{S4})$$

where $\delta(\mathbf{r}, \mathbf{r}_{ijk})$ is the discretized delta function (1 if we're treating \mathbf{r}_{ijk} as the same location as \mathbf{r} for visualization purposes, otherwise 0). The color representations for the animations are proportional to $\bar{z}(\mathbf{r})$ normalized to the highest charge density at that frame's potential.

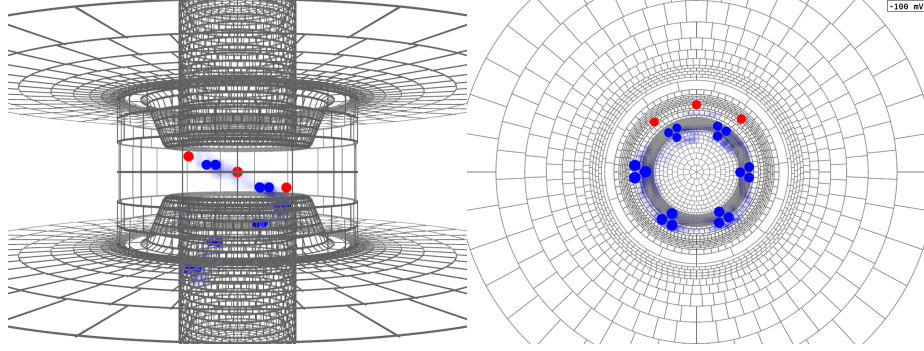


Figure S3: *Standard α -helical model*: (See Movie S1). Position and distribution of charges for model α (1) in Table 1B with $\epsilon_p = 4$. Red symbols represent fixed negative counter-charges, blue symbols represent the mean position of $-1/3 e_0$ on S4 arginines, and blue shading represent the relative probability of negative charge at a given position. This is the model used in Fig. 3A.

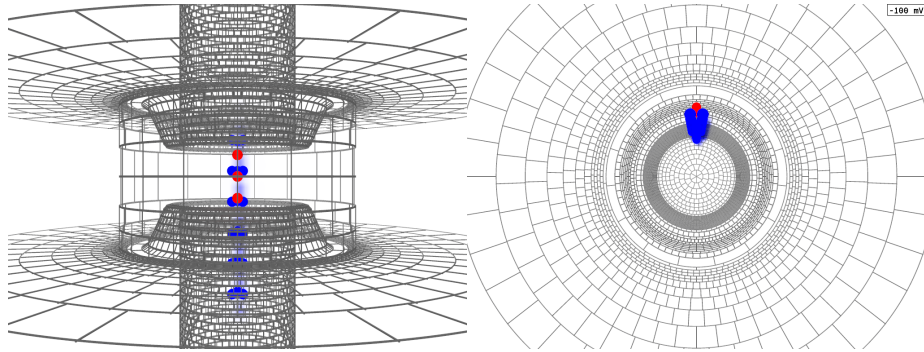


Figure S4: *Standard 3_{10} -helical model*: (See Movie S2). Position and distribution of charges for model 3_{10} in table 1B with $\epsilon_p = 4$. See the description of Fig. S3 for further details. This is the model used in Fig. 3B.

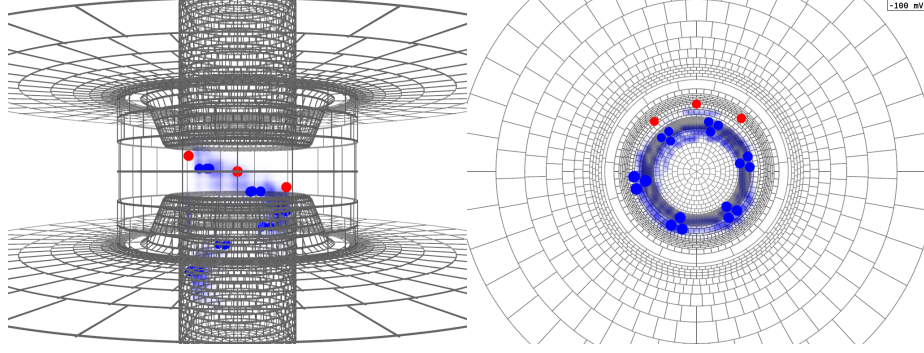


Figure S5: α -helical model with $\epsilon_p = 16$: (See Movie S3). Position and distribution of charges for model α (1) in table 1B with $\epsilon_p = 16$. See the description of Fig. S3 for further details. This is the model used in Fig. 7.

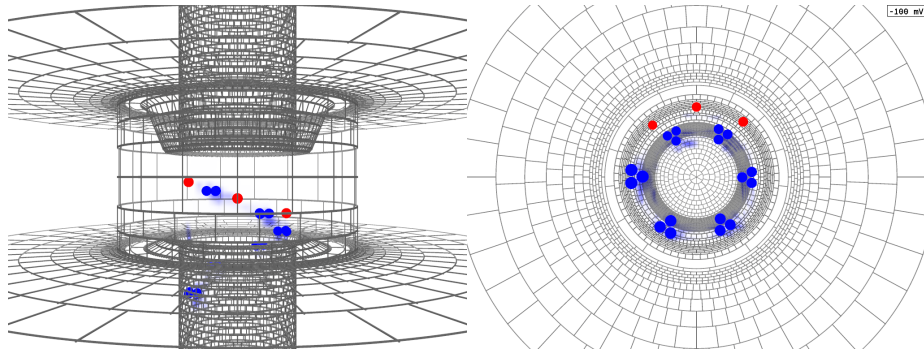


Figure S6: α -helical model with asymmetric gating canal: (See Movie S4). Position and distribution of charges for model α (4) in table 1B with $\epsilon_p = 4$. See the description of Fig. S3 for further details. This is the model used in Fig. 8, outline 4.